Available online at www.sciencedirect.com
SCIENCE DIRECT
C. R. Physique 5 (2004) 753–767
COMPTES RENDUS PHYSIQUE

Ice: from dislocations to icy satellites/La glace : des dislocations aux satellites de glace

Fracture of the winter sea ice cover on the Arctic ocean

Erland M. Schulson [a,*], William D. Hibler III [b]

[a] *Thayer School of Engineering, Dartmouth College, Hanover, NH 03755, USA*
[b] *International Arctic Research Center, University of Alaska, Fairbanks, AK 99775, USA*

Available online 6 October 2004

Presented by Guy Laval

Abstract

We account for the brittle behavior of the winter sea ice cover in terms of the competition between creep relaxation and crack extension at stress concentrators; identify as Coulombic shear faults sliding lineaments that lace through the cover; and numerically model fault development in terms of scale-independent effective friction. ***To cite this article: E.M. Schulson, W.D. Hibler III, C. R. Physique 5 (2004).***

Résumé

Fracture de la banquise en hiver. On propose une interprétation du comportement fragile de la banquise (en hiver) en termes de compétition entre extension d'une fracture à partir de concentrateurs de contraintes, et relaxation de ces concentrations de contrainte par fluage. On identifie les zones de glissement intense qui s'entrelacent à la surface de la banquise comme étant des failles cisaillantes de Coulomb, et on modélise numériquement le développement de ces failles en termes de friction effective indépendante de l'échelle spatiale considérée. ***Pour citer cet article : E.M. Schulson, W.D. Hibler III, C. R. Physique 5 (2004).***

Keywords: Winter sea ice cover; Creep relaxation; Crack extension; Coulombic shear faults

Mots-clés : Banquise ; Relaxation de ces concentrations de contrainte ; Extension d'une fracture ; Failles cisaillantes de Coulomb

1. Introduction

The ice cover on the Arctic Ocean plays a significant role in both local and global climate. It reflects solar radiation, impedes the transfer of heat from the ocean to the atmosphere and, during formation, contributes to oceanic salt flux and thus to ocean currents. The ice thickness is a key factor in each of these processes and therein lies the interest in fracture.

The ice cover is a dynamic body, moving under the action of wind and ocean currents [1]. Gradients in velocity induce internal stresses which, when large enough, generate a ubiquitous network of cracks and leads. Through the leads enough heat escapes to dominate the ocean-atmosphere exchange during winter [2]; within them more salt is rejected as new ice forms; and as they close, the new ice breaks into blocks that pile up and push down to form pressure ridges, which by some estimates [3] can account for $\sim 50\%$ of the floating ice mass. Fracture is thus a fundamental process in the ice thickness distribution.

In this article we address the brittle versus ductile character of the cover; consider the nature of long, linear faults that run hundreds and thousands of kilometers through it; construct a theoretical model for the orientation of the macroscopic faults; and

* Corresponding author.
E-mail address: erland.schulson@dartmouth.edu (E.M. Schulson).

1631-0705/$ – see front matter
doi:10.1016/j.crhy.2004.06.001

then present some numerical modeling of fault evolution and orientation. Also, we present evidence that the physics of fracture is scale independent.

2. Ductile-to-brittle transition

Why does the sea ice cover behave in a brittle manner? One might have thought that a floating plate whose average temperature is $> 90\%$ of its melting point and which deforms rather slowly at about 1%/day or 10^{-7} s^{-1} [4] would creep in the way that glaciers do, instead of breaking up. The answer, we think, can be found in a simple model of the ductile-to-brittle transition [5,6]. The idea is that macroscopic inelastic behavior is governed by a competition between two processes: the development of internal stress as the body deforms under external forcing, and the relaxation of those stresses through viscous flow. The first dominates under higher loading rates and results in the building up of stress to the point of triggering fracture. The second process dominates under lower loading rates and leads to macroscopically ductile behavior. The ice cover, as we show below, appears to deform too quickly for creep relaxation to govern its behavior.

Imagine a cover replete with weaknesses such as thermal cracks and other flaws [7], loaded under compression and stabilized against buckling by its thickness (1.8 m to 2.8 m: [3,8,9]). We specify a compressive stress state, because in-situ stress measurements during winter [10,11] show that macroscopic failures are driven primarily by compressive stresses. As load rises, say during the passage of a weather system, theory holds [12–16] that the ice begins to slide across favorably oriented flaws. This relative movement changes the stress state locally, from compressive to tensile, as well as concentrating the stress either at the tips of the flaws or, should the displacement occur non-uniformally, along one side of them. Under low rates of loading, material within the tensile zones creeps sufficiently to allow the stresses to relax, and ductile behavior ensues. Under higher rate, on the other hand, local tension builds to the point of initiating secondary cracks, termed wing cracks (from the tips) and comb cracks (from the sides), Figs. 1 and 2. We hypothesize that when the size of the region, r_c, within which the viscous strain exceeds the elastic strain is smaller than a certain fraction, f, of the length of the parent flaw, $2a$, the secondary

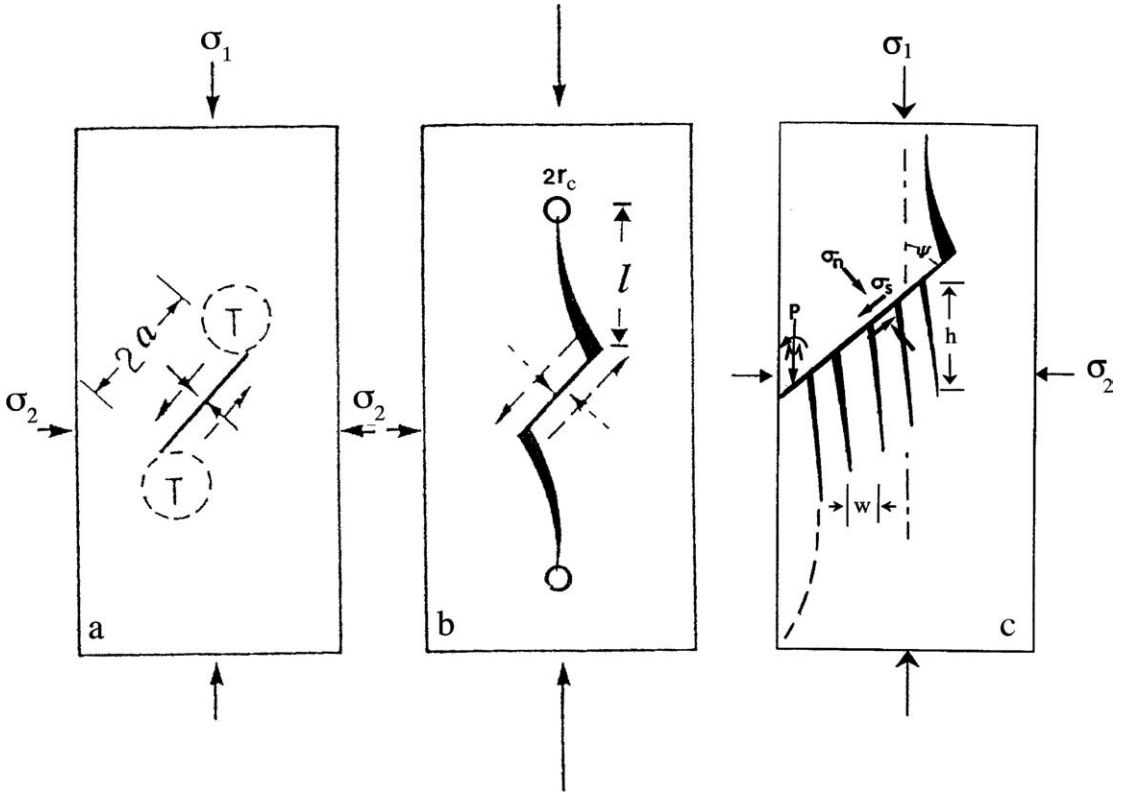

Fig. 1. Schematic sketch showing the formation of secondary cracks from sliding along parent flaws under an applied compressive stress: (a) pre-secondary build-up of localized tension at tips of the parent flaw; (b) wing cracks sprouting from the tensile zones in (a); (c) comb cracks sprouting from one side of the parent flaw (from [6,22]).

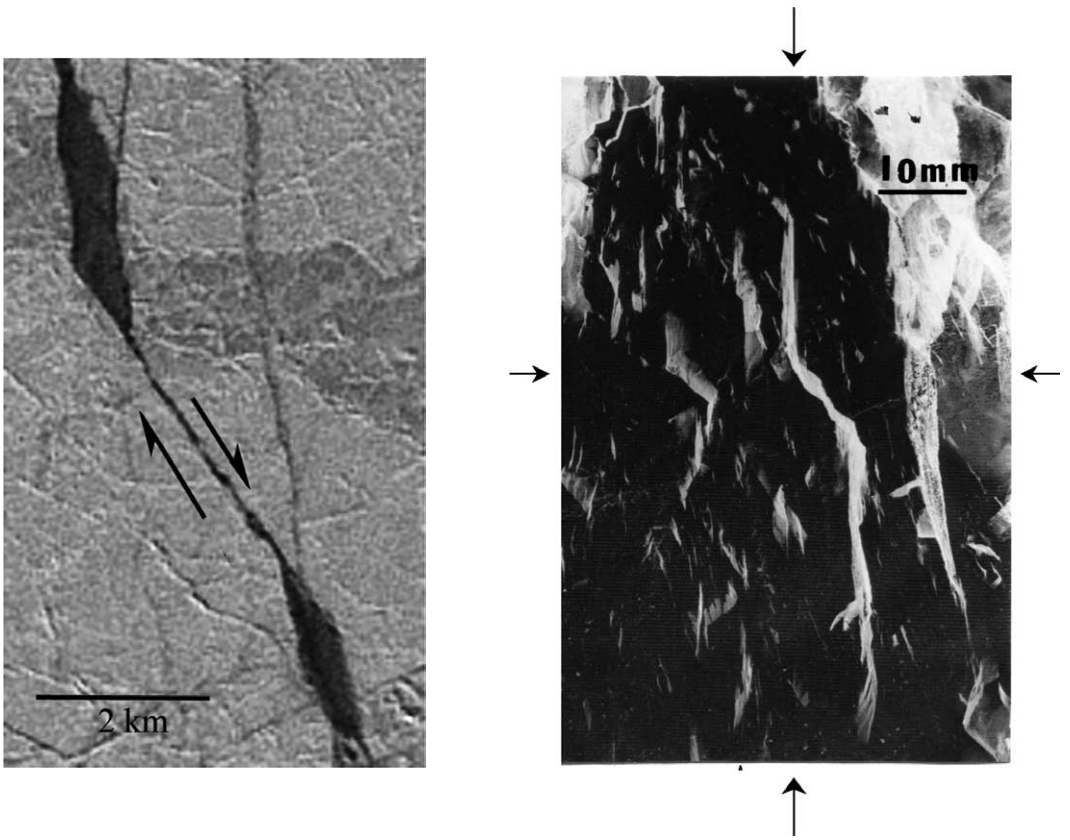

Fig. 2. Wing cracks: (a) from near the southern tip of L5 in Fig. 3; (b) within a test specimen of columnar ice loaded in the laboratory ($-10\,^{\circ}$C) to terminal failure under moderate biaxial confinement.

cracks lengthen in a direction parallel to the direction of the greatest compressive stress and then interact to create macroscopic splits [5]. We thus take as the criterion for the ductile-to-brittle transition the equality $r_c = 2fa$. By applying the Riedel–Rice [17] analysis of crack-tip creep to calculate r_c, and the Ashby and Hallam [15] analysis of sliding cracks to determine the crack-tip loading rate, we can show that the transition strain rate is given by the relationship [6]:

$$\dot{\varepsilon}_t = \frac{BK_{Ic}^3}{f(2a)^{1.5}\{[1+\mu^2]^{0.5} - \mu - R[\mu + (1+\mu^2)^{0.5}]\}}, \tag{1}$$

where B is the temperature-dependent constant in the power law creep equation $\dot{\varepsilon} = B\sigma^n$ (where $\sigma = [\sigma_1^2 - \sigma_1\sigma_2 + \sigma_2^2]^{0.5}$ and where σ_1 and σ_2 are the maximum (taken in this paper as the most compressive stress) and minimum principal stresses, respectively, and where $n = 3$), K_{Ic} is fracture toughness, $R = \sigma_2/\sigma_1$ and μ is the coefficient of sliding friction.

It is not easy to test this model by performing systematic experiments on floating ice covers. Instead, we tested it in the laboratory through experiments on sub-meter sized specimens in which cracks along millimeter-sized grain boundaries serve as the stress concentrators [5,6,18–20]; for review see [6]. That sliding along short parent cracks generates secondary cracks as well is evident from Fig. 2. Indeed, it was on the small scale that wing cracks were first observed [21]. The experiments showed that the transition actually occurs over a narrow range of strain rate, but that the average rate is around 10^{-4} s^{-1} to 10^{-3} s^{-1} in good agreement with the model. We have also tested a more recent derivative against the ductile-to-brittle transition in a variety of rocks and minerals and again found that it worked reasonably well [22].

The concepts underlying the model are not specific to material or to spatial scale. It seems reasonable, therefore, to apply it to the sea ice cover. If we take the average ice temperature to be about $-20\,^{\circ}$C and employ parametric values for that temperature (albeit, values obtained from measurements on smaller specimens) $B = 5.1 \times 10^{-6}$ MPa^{-3} s^{-1} [23], $K_{Ic} = 0.2$ MPa m$^{0.5}$ [24], $\mu = 0.5$ [25], $f = 0.02$ [18], and if we assume a moderate confinement of $R \sim 0.1$, then we obtain the 'scaling law':

$$\dot{\varepsilon}_t a^{1.5} = 2 \times 10^{-6}\ \text{s}^{-1}\,\text{m}^{1.5}, \tag{2}$$

where the half-length of the parent flaws, a, is given in meters and the strain rate in s^{-1}. The average strain rate of the ice cover and the distribution about the average depend upon spatial scale: both parameters increase as the scale decreases, the latter more so than the former [26]. For the present purpose, we note that the deformation rate ranges from 10^{-8} s^{-1} to 10^{-6} s^{-1} at the 10 km scale [26], and so we work with those numbers. Eq. (2) then implies that flaws must be > 60 meters in length to account for the brittle behavior at the lowest rate. Given the fact that thermal cracks can be tens to hundreds of meters in length [7] or even longer (Coon, 2003, personal communication), and given the likelihood that healing of partially-through-cover cracks is impeded by brine drainage into them (Coon, 2003, personal communication), this requirement would seem to be easily met. The 'law', incidentally, is not expected to be very sensitive to temperature – and this has been shown to be true on the laboratory scale [27] because B and μ respond in an opposite sense to this parameter. Nor is it expected to be very sensitive to confinement.

We have, then, a quantitative description of the ductile-to-brittle transition that is based upon conventional creep and fracture mechanics. While simplistic in that it ignores primary and tertiary creep, crack interactions, heterogeneities, as well as possible differences in materials properties between the field and the laboratory, the model offers for the first time an account of the macroscopic behavior of an ice sheet in terms of independently measurable physical parameters.

Before leaving the subject, we note that the transition strain rate is relatively low. One of the reasons is that as a material ice exhibits relatively high creep resistance. This is evident from the fact that at 90% of its melting temperature under a shear stress of $10^{-4}G$, where G is the shear modulus, ice creeps at $\sim 10^{-8}$ s^{-1}. This is to be compared with a creep rate of $\sim 10^{-3}$ s^{-1} for elemental nickel and for the mineral wustite (FeO) at the same normalized temperature and stress [28]. The low rate results from the fact that dislocations within the ice Ih crystal structure glide rather sluggishly through the lattice [29] owing, it has been suggested [30], to the unique requirement of protonic rearrangement. Another reason for the low transition strain rate is that the fracture toughness of ice is amongst the lowest of all materials.

3. Long linear fracture features: compressive shear faults

We turn next to what are arguably the most significant fracture features within the winter ice pack; namely, long narrow lineaments which lace through the ice and run for hundreds and sometimes thousands of kilometers through the Arctic Basin [4,31–41]. The lineaments recur year after year and appear to be composed of kilometer-wide bands of damage which often intersect in an acute angle (typically $2\theta \sim 20^\circ$ to 40° to form diamond-shaped patterns. These features mark zones where velocity gradients are spatially discontinuous [34,38,39] and thus where shear and/or divergence as well as vorticity are concentrated. For this reason they have been termed 'slip lines' [32,40], although this appellation perhaps could be misleading since the term more conventionally implies volume-conserving, von-Mises plasticity. A better term is 'linear kinematic feature' or LKF [4], albeit less-specific. In effect, lineaments divide the cover into semi-rigid plates or parts of plates which move apart or wedge open to allow new ice to grow and then move together to create pressure ridges, as noted in the Introduction. How they form is the issue.

Before addressing that question, consider the following observations [41]. Fig. 3 shows a high-resolution (29 meter pixel size) Landsat-7 image taken within the visible band on 25 March 2000. The scene is within the pack ice near the Canadian Archipelago and encompasses an area 183 km wide (ENE-WSW axis) $\times$170 km long (NNW-SSE axis). Fifteen of the more prominent lineaments are sketched and labeled in Fig. 3(b). (Although labeled separately, L2 and L10 may be part of the same fracture zone.) With the exception of L1–L3 and L10, they all exhibit a strong N–S component to their orientation and several intersect at an average acute angle of $2\theta = 38^\circ \pm 5^\circ$, like those reported earlier [37]. Large, rhomboidal-shaped openings punctuate L6, L15 and L4 and smaller ones punctuate most of the other lineaments, signifying shear displacements of either right-lateral (R-L) character (L4, L7, L8, L12 and L13) or left-lateral (L-L) character (L5, L6, L14 and L15). The wing-like crack shown in Fig. 2(a) is from the region near the southern tip of L5, and others are distributed here and there throughout the field of damage. The wings are oriented mainly in a N–S direction which we take to coincide with the direction of maximum principal stress, σ_1, at the time the damage formed. From wing crack mechanics [15]):

$$\sigma_1 = \frac{K_c\sqrt{L}}{\sqrt{\pi a}(.23(1-\mu))}, \tag{3}$$

where $L = l/a$ and where l the length of the wing as defined in Fig. 1. Using the same parametric values as above and for the crack shown in Fig. 2(a), for instance ($a \sim 2$ km, $L \sim 2$), we obtain $\sigma_1 \sim 40$ kPa. This estimate is bracketed by actual in-situ measurements of ice sheet failure stresses during earlier winters, which generally fall within the range 10 kPa to 100 kPa [10,11].

We thus interpret the recurring long, sliding lineaments to be compressive shear faults oriented about the direction of maximum compressive stress. Fig. 3(c) shows a conjugate set. They are analogous to strike-slip faults within the Earth's crust, a point first noted by Marko and Thomson [31]. They form, we propose, through the linking-up of en echelon arrays of secondary cracks, Fig. 4. While detailed studies of their evolution remain to be made, Kwok's (2003) SAR-RADARSAT observations

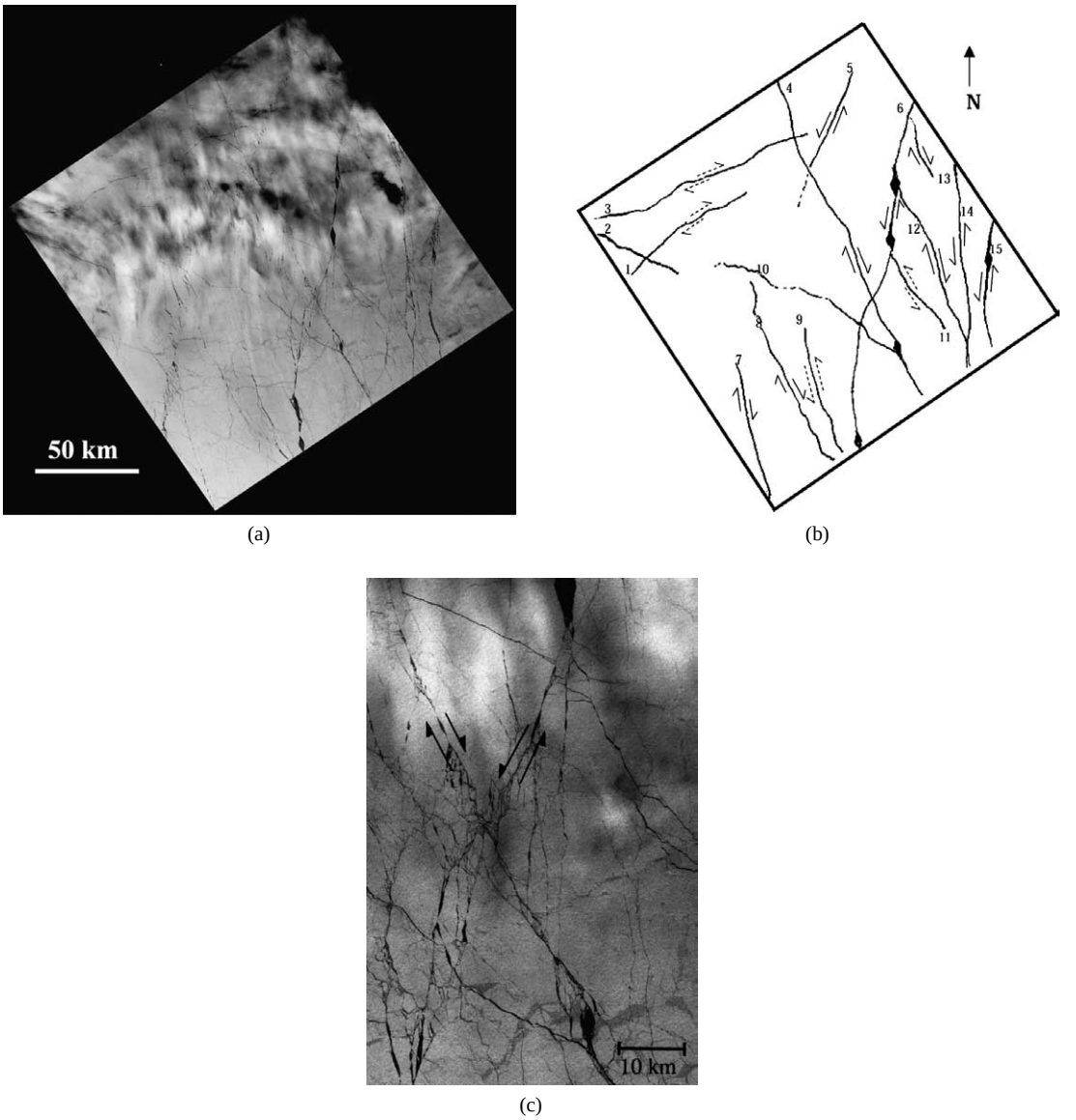

(a) (b)

(c)

Fig. 3. (a) Landsat-7 image of the sea ice cover on the Beaufort sea, 25 March 2000 centered approximately at 80.0 °N/135.7 °W. North is up. The spatial scale is an average of the horizontal and vertical scales. The secne encompasses an area of 183 km wide (ENE-WSW axis) ×170 long (NNW-SSE axis). (b) Schematic sketch of (a) where the most prominent lineaments are labeled L1–L15. The arrows denote either right-lateral or left-lateral relative movement. (c) Higher-magnification image of (a) showing the intersection of L4 and L6.

during the SHEBA (surface heat energy budget in the Arctic) experiment [42] appear to support the proposed mechanism. Fig. 5 shows his record of the development of a set of sub-parallel, shear-fault features during the two-week period 30 October to 11 November 1997. During the three-day interval between 11 November and 14 November two major L-L faults (A–A′ and B–B′) formed and were oriented in approximately the NE–SW direction. The faults appear to be made up of individual wing cracks. Their character is especially evident from the narrower fault, B–B′ where, owing to a lower degree of divergence (0.029 versus 0.11, [41]), the cracks are less distorted than they are along fault A–A′. Again, from the orientation of the wings we deduce that at the time of faulting the maximum compressive stress within the cover acted along a direction rotated counter-clockwise by $\sim 30°$ from the strike of the faults. From the geometry of the wings ($a \sim 1$ km and $L \sim 3$) we estimate (using Eq. (3) and the above materials parameters) that $\sigma_1 \sim 19$ kPa. Encouragingly, this estimate compares favorably to a stress spike of ~ 30 kPa (compressive) that was measured by Richter-Menge et al. [10] at the SHEBA site around mid-November 1997 when the faults first formed.

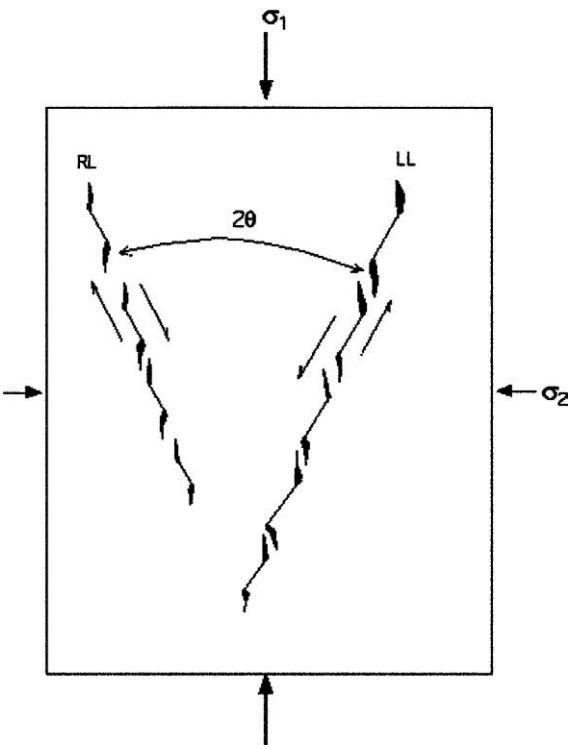

Fig. 4. Schematic sketch showing the formation of a compressive shear fault through the proposed linking up of secondary (wing) cracks.

Further insight must await additional studies. In the meantime, it is interesting to note that laboratory studies (for review see [6]) have revealed deformation features – wing cracks, comb cracks and conjugate compressive shear faults accompanied by rhombohedral openings – that closely resemble the larger-scale features described above. Fig. 2, for instance compares wing cracks on the two scales and Fig. 6 shows shear faults produced under biaxial compressive loading [43]. Does this 'look alikeness' mean that the fracture mechanisms are basically independent of spatial scale? When combined with earlier observations [6,44] and with recent fractal analysis [45,46], we think it does.

We are aware that our hypothesis of scale independence is controversial. Other investigators [47] take the opposing view, citing as evidence the fact that the failure stress of an ice sheet is about a factor of 10^3 lower than that of a laboratory specimen [23]. Instead, they [47,48] invoke hierarchy theory [49] and argue that it is the degree of disconnectedness between scales that accounts for the organization of the system. The problem with the hierarchy approach is that the different scales (e.g., floe scale < 1 km; multi-floe scale 2–10 km, and so on) seem to be defined rather arbitrarily. Also, the approach seems to contradict the observation [45] of no characteristic length in the pattern that accompanies the fracture and fragmentation of ice in nine orders of magnitude, from 10^{-4} m to 10^5 m. As to the difference in strength, that observation can be accounted for simply in terms of the difference in size of the stress concentrators; i.e., $\sigma_{\text{lab}}/\sigma_{\text{field}} = (a_{\text{field}}/a_{\text{lab}})^{0.5} = (\text{kilometer/millimeter})^{0.5} = 10^3$. It might also be accounted for in terms of the limited temporal resolution (5 min to 1 hr) of the in-situ stress measurements [10,11] and in the possibility of that very short-term, higher-stress events were not recorded.

In identifying sliding lineaments as compressive shear faults, we distinguish them from another kind of fault that can occur in ice, at least in the laboratory [50]. The other kind is oriented at $\sim 45^\circ$ to the principal directions, is narrower, is attended by little or no volume change, and leads to pressure-insensitive terminal failure as opposed to pressure-hardening. For those reasons we term this second kind of fault a plastic or P-fault and term the ones with which we are concerned in this paper Coulombic (i.e., frictional) or C-Faults. P-faults form under triaxial compressive stress states when the hydrostatic component of the stress tensor becomes large enough to suppress frictional sliding across crack faces [50]. Given the predominantly biaxial character of the stress state within the sea ice cover, P-faulting is unlikely to contribute to failure there.

4. A rate-independent effective friction model for Coulombic faulting

To translate the failure mechanisms and observations described above into a mathematical form suitable both for numerical modeling and for interpreting numerical simulations, we develop an idealized model of the failure zone in a heterogeneous

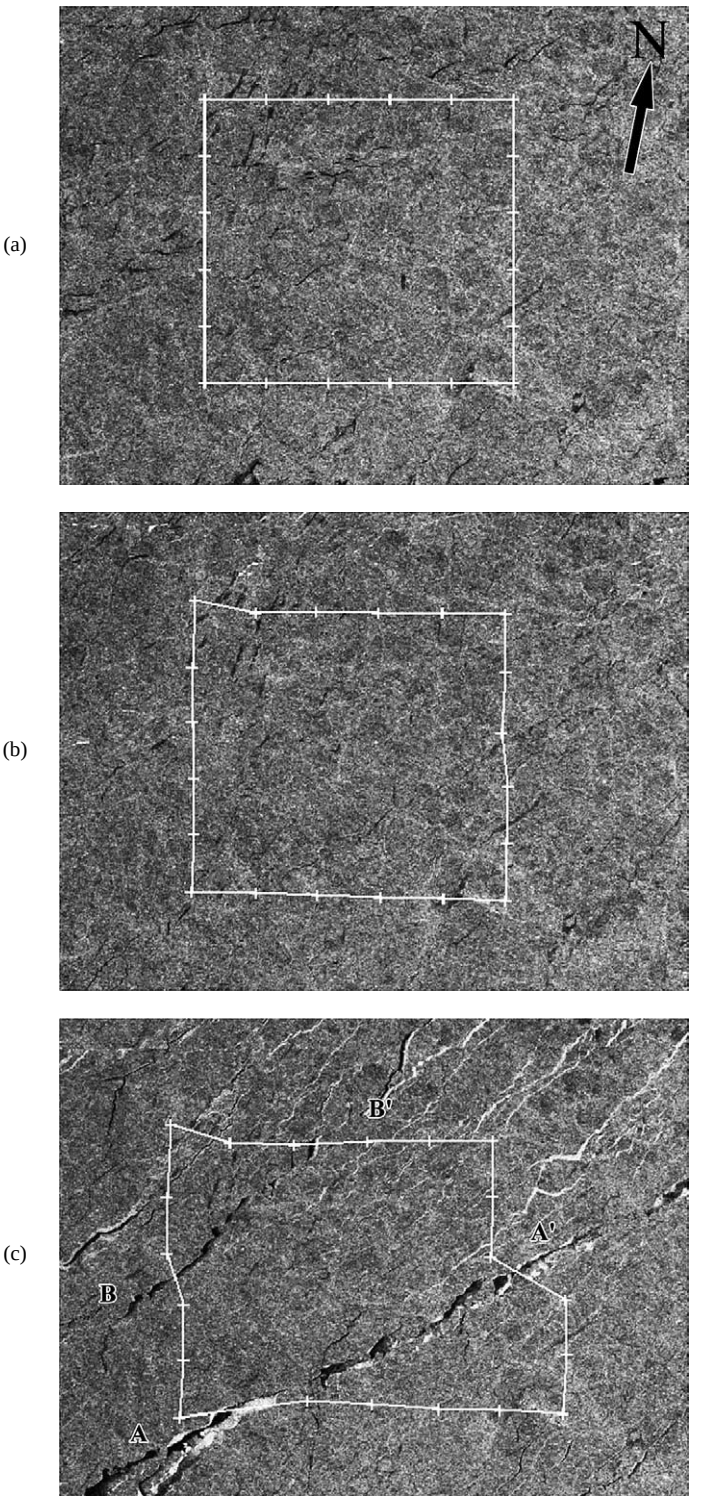

Fig. 5. SAR-RADARSAT images of sea ice taken during the SHEBA field experiment, courtesy of Dr. R. Kwok of Jet Propulsion Laboratory and Dr. Harry Stern, Applied Physics Laboratory, University of Washington. RADARSAT imagery (Copyright CSA 2002). (a) RADARSAT image from day 302, 1997. The scale of the grid is 10 km/division. (b) RADARSAT image from day 314, 1997. (c) RADARSAT image from day 317, 1997. Note the two left-lateral shear faults A–A′ and B–B′, the 'closed' wing cracks on fault-B–B′ near to its intersection with the northern border of the grid, and the rhomboidal openings along the more open fault A–A′.

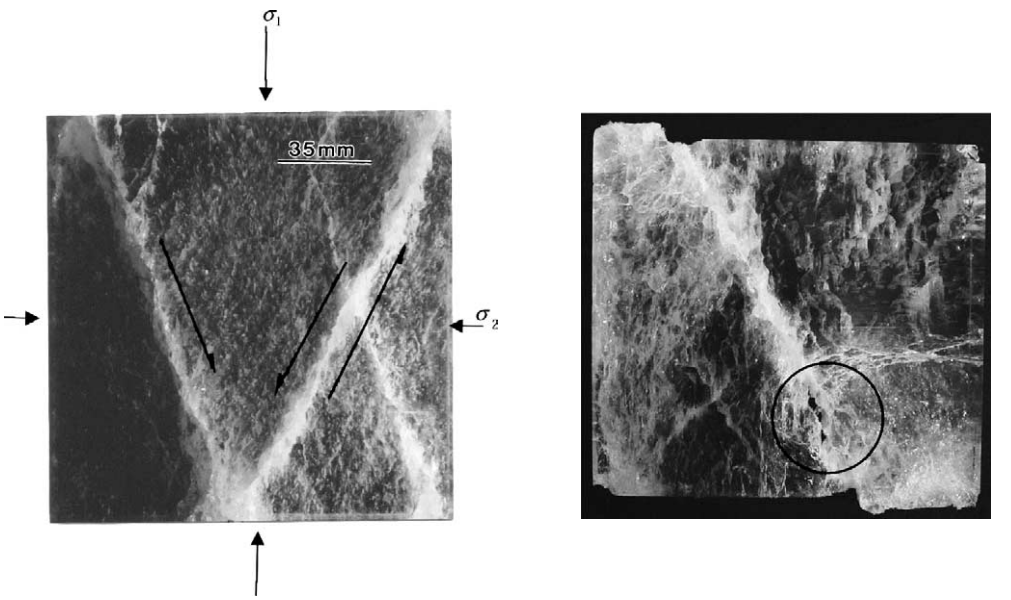

Fig. 6. Photographs showing brittle compressive deformation features in columnar S2 ice biaxially loaded across the columns (running in and out of the plane of the paper) to terminal failure in the laboratory at −10 °C: (a) showing conjugate sets of shear faults; (b) showing a right-lateral shear fault in a specimen that was slid 10 mm over the fault, creating a rhomboidal opening (circled) along it.

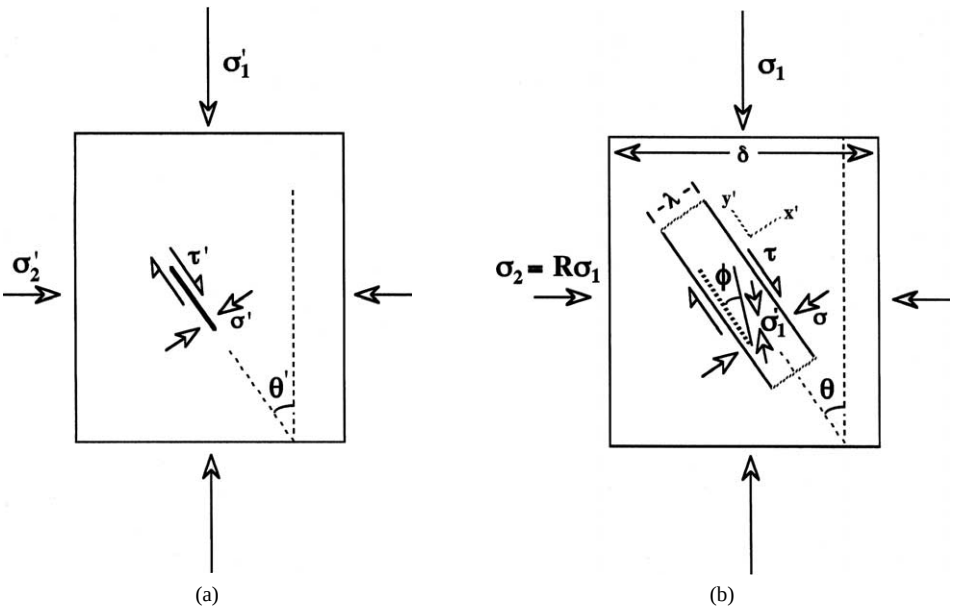

Fig. 7. Schematic sketches showing: (a) local sliding friction model; and (b) 'effective friction' Coulomb fault model.

ice cover. The essential idea is that material within the fault may be described by a rate-independent failure envelope that is derivable from laboratory observations. To a large degree the mathematics turn out to be equivalent to the sliding friction model shown conceptually in Fig. 7(a), except that there is now dilatation and an effective friction coefficient μ_e which is dependent upon the flow rule and the failure criterion of the material within the Coulombic fault itself. While the mechanism described above provides a description of fault formation, it does not directly provide a basis for predicting the orientation of failure zones formed in pack ice under a variety of wind and water forcing conditions. One of the main purposes of this 'effective friction' model, therefore, is to provide scale-invariant predictive capability.

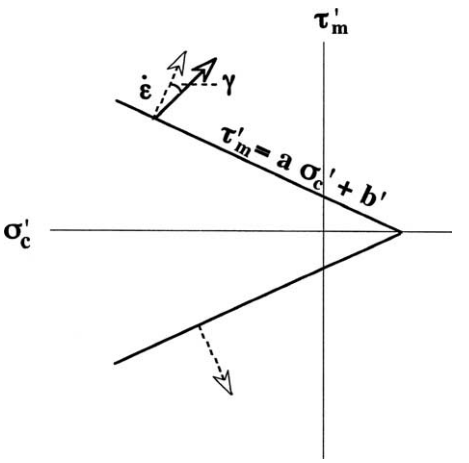

Fig. 8. Principal space fixed flow rule failure envelopes used in the failure zone in Fig. 7(b). The dilatation angle, γ, is the angle between dilation-free shear flow shown by the solid vector and the fixed angle flow rule (not necessarily normal) shown by the dashed vector. In the case of a zero dilatational angle the yield curve follows from the sliding friction model in Fig. 7(a).

Consider a region of pack ice of dimension δ with average boundary contact stresses of σ_1 and σ_2, Fig. 7(b). We consider δ to be small compared to the spatial variation of wind and water body forces. Within this region we imagine the stresses to introduce a small amount of strain which is concentrated in a failure zone of width λ where $\lambda \ll \delta$. This failure zone is formed by linking weaknesses in the ice, as described above, and is taken to be present at all scales and certainly at scales smaller than typical failure zones in pack ice. Our idealization is that the failure zone is a region of weak ice surrounded by stronger rigid ice and is mathematically equivalent to the oriented lead model proposed earlier [51]. The orientation, ϕ, of the principal stresses in the failure zone (Fig. 7(b)) is dictated by the flow characteristics of the material there. In other words, we assume that the deformation of the ice cover is intrinsically heterogeneous and that it consists of material in two states (Fig. 7(b)), 'virgin' and 'damaged', each with its own rheological behavior. A classical analysis assumes only 'virgin' material with a planar crack or weakness (Fig. 7(a)).

To determine the fault orientation, we imagine that the damage band forms at an angle, θ, relative to the principal stress axes in such a way that the stress is minimized. Since the failure band is narrow, the stresses in the rigid portion of the ice and the fault are taken to be constant and necessarily equal only along the common fault faces. Because the band is assumed to be undergoing failure with a failure envelope and flow rule similar to those for the rigid ice, the orientation may be obtained by matching stresses at the rigid ice/fault boundary. We consider the material in the band to obey a failure criterion characterized by variable dilatation and by variable friction. A simpler criterion, with fixed friction and no dilatation, is shown in Fig. 8. By rotating the stresses within the failure zone to a co-ordinate system aligned with the zone and by equating the shear and compressive stresses across the fault face, we obtain [51]:

$$\frac{1+R}{2}\sigma_1 - \sigma_1\frac{1-R}{2}\cos(2\theta) = \sigma_1\frac{1-R}{2}\sin(2\theta)\left[\frac{1-a\cos(2\phi)}{a\sin(2\phi)}\right] - \frac{b'}{a}, \tag{4}$$

where again $R = \sigma_2/\sigma_1$, a and b' are constants (see Fig. 8) specified by the internal friction angle and cohesion of the material in the failure zone, respectively, ϕ is an angle dictated by the dilation angle, γ (see Fig. 8), and the various stresses are defined in Figs. 7 and 8. Minimizing σ_1 with respect to θ, we obtain in the special case of ϕ constant (fixed γ) a preferred flaw orientation independent of confinement ratio [51]:

$$\tan(2\theta_c) = \pm\frac{1-a\cos(2\phi)}{a\sin(2\phi)} = \frac{1}{\mu_e}, \tag{5}$$

where μ_e is an effective friction coefficient of the composite and probably differs from the coefficient defined in Sections 2 and 3. Upon substituting this result into Eq. (4) we obtain:

$$\frac{\sigma_1+\sigma_2}{2} = \frac{\sigma_1-\sigma_2}{2}\cos(2\theta_c) + \frac{b'\cos(2\theta_c)}{a} \tag{6}$$

which represents the relationship between the maximum shear and compressive stresses at the minimum failure stress.

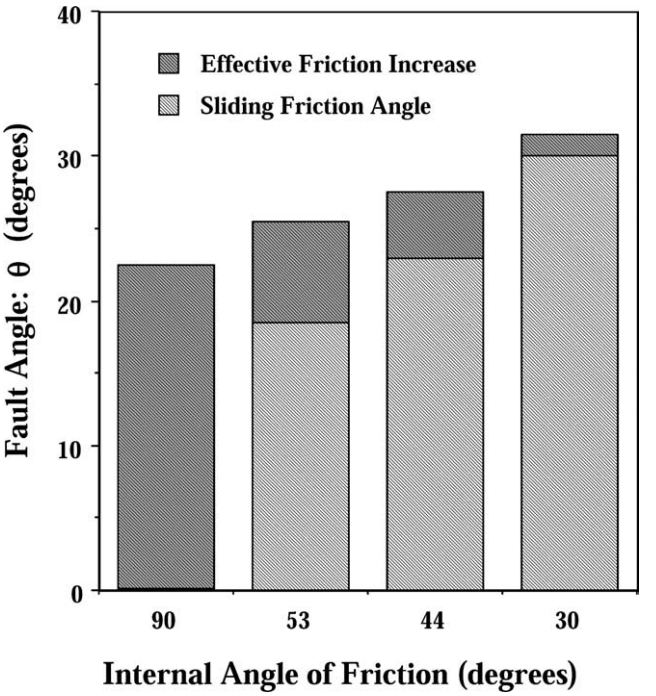

Fig. 9. Angle of stress characteristics or expected fault angle (θ in Fig. 7(a)) for sliding friction model; and increase of fault angle for effective friction coulomb band model in Fig. 7(b) based on using a sliding friction model within the narrow band. The internal angle of friction (b) is related to a friction coefficient μ by $\mu = \tan(\beta)$. For a positive dilatation angle the increase of fault angle will be less pronounced for the 'Coulomb fault' model.

In the case of the sliding fixed-friction model, Fig. 7(a), we adopt the Coulombic failure criterion for the depicted flaw to be $\tau' = \mu\sigma' + b$ where b is a measure of cohesion. By a similar analysis to the one above we obtain:

$$\tan(2\theta'_c) = \pm\frac{1}{\mu} \tag{7}$$

with the relationship between shear stress and compressive stress for $\theta' = \theta'_c$ given by:

$$\frac{\sigma'_1 + \sigma_2}{2} = \frac{\sigma'_1 - \sigma'_2}{2}\cos(2\theta'_c) + \sin(2\theta'_c)b. \tag{8}$$

Except for constant factors in the cohesion term, the failure band model is mathematically equivalent to the sliding friction model in terms of the stress equations, except that an effective friction term now appears. The one case where the effective friction equals the sliding friction occurs when a normal flow rule is assumed. This case can be verified by determining the principal axes of the stress in the fault from the strain rate there [51].

An independent mathematical justification for the fault orientation may be obtained by the method of characteristics. It is well known that for a material having the characteristics described by Fig. 7(a) with the local failure relation $\tau = \mu\sigma + b$, the mathematical 'stress' characteristics of the equations of motion are identical in orientation and character to angle given in Eq. (6). This may be seen by considering the stresses obeying Eq. (6) or Eq. (8) in an arbitrary co-ordinate system rotated at some angle β relative to the orientation of the 'minimum stress' failure band, which for the purpose of the 'characteristic calculation' is simply a suitable reference angle. All components of the stress may then be written in terms of σ'_c and β which then become the dependent variables. Writing Euler's equation of motion (gradient of the stress equals the net body force) in a Cartesian co-ordinate system in terms of x and y derivatives of σ'_c and β, one can see that the equation is hyperbolic with intersecting characteristics at $\pm\theta'_c$ as defined in Fig. 7 and Eq. (7).

Consequently by either the physical argument or the 'characteristics' argument, the failure zones for a material exhibiting rate-independent failure, such as described by Eq. (6), are mathematical stress characteristics along which failure would be expected to occur. Because the effective angle of friction is different, these faults for the 'idealized Coulombic fault model' will have larger intersection angles, a comparison of which is shown in Fig. 9 for the case of shear flow with no dilation. In particular, in the case of very large friction, the intersection angle, 2θ, may be 45° as compared to zero for the sliding friction model.

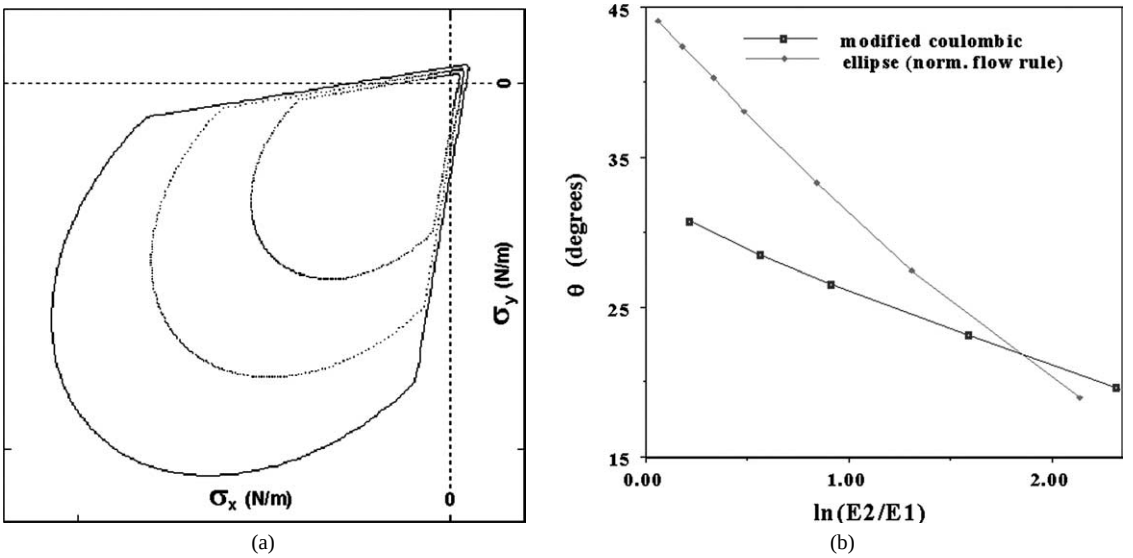

(a) (b)

Fig. 10. (a) Modified Coulombic failure envelope [51] based on experimental measurements [19] with non-normal flow rule. (b) Expected fault angles for fixed principal axis strain rate ratios ($E1 = |\dot{\varepsilon}_1|$, $E2 = |\dot{\varepsilon}_2|$) based on minimizing deformational energy [52].

Where more complex rheological behavior applies to the failure band with either variable dilatation and/or variable internal friction, it is difficult to estimate the failure stresses analytically. However, a numerical solution [51] may be carried out by specifying a confinement ratio and one component of strain along the principal stress direction. The second component of strain is adjusted, in an exact analog to the laboratory [19], to keep the confinement ratio fixed in the numerical experiment. With typical non-normal flow rules these numerical results yield fault angles different from those based on the internal friction angle of the rheology of the fault. For example, using the modified Coulombic yield curve shown in Fig. 10(a) with a variable flow rule, the expected fault angles for opening failure range from zero to $\sim 30°$. In the case of a normal flow rule, the stresses in the fault and the rigid ice are identical at the critical fault angle.

Numerical results [52] also show that for fixed ratio of strain rate, the orientation of the fault may be found by minimizing the dissipational energy as a function of θ. This minimum energy argument is particularly useful for interpreting orientations of failure zones simulated in high-resolution, large-scale models with either idealized or more realistic wind and current forcing. In such model simulations, as shown in the next section, heterogeneities in the ice cover lead to only opening faults due the necessity of weakening the cover as weaknesses link up. By applying this energy minimization principle to symmetric faults and using the modified Coulombic rate-independent behavior (Fig. 10(a)) assumed by Hibler and Schulson [51], we find $\theta \sim 30°$ for the limit of zero-dilation shear, Fig. 10(b), whereas we obtain $\theta \sim 45°$ when using an elliptical rate-independent failure envelope [52].

5. Numerical simulation of multiple and conjugate faults

When appropriate forcing and heterogeneity of ice strengths are applied to a numerical simulation, single or intersecting failure zones develop. The formation of the zones closely mirrors the evolution of Coulombic faults as described in the first sections of this paper, inasmuch as zones of weakness form and thereby germinate points for propagating weaknesses which can then ultimately lead to connected oriented bands of weaker ice. Once the zones form in a numerical model, they effectively represent finite-width failure bands, which by the consistency of the numerical model formulation are guaranteed to have continuity of stresses along common faces. Consequently, the application of the Coulomb fault model by stress characteristics or deformational energy minimization should predict fault orientation.

We take the rheology in the fault to be similar to that given by laboratory measurements [19] which we parameterize with a flow rule as described elsewhere (see Appendix A [51]). The simplest application is to consider a uniform deformation field with a single center weakness forced by stresses at the boundary (Fig. 7). Stresses with a given confinement ratio are specified at the boundary and steady-state failure experiments are performed without weakening until stresses adequate enough to cause the propagation of failure almost (but not all the way) through the sample are reached. Two such cases for different confinement ratios are shown in Fig. 11(a) and (b). In agreement with expected angles for this particular failure envelope, a

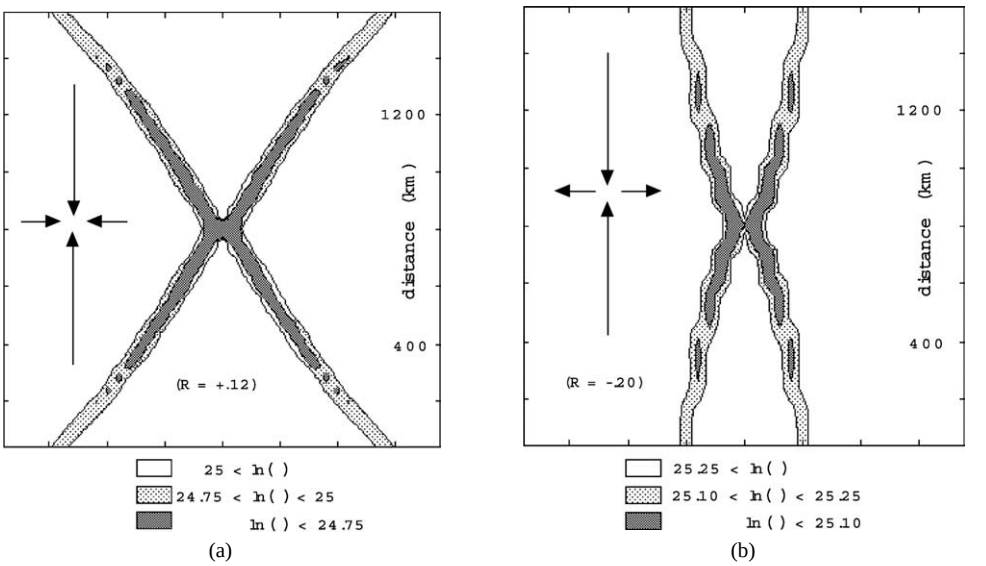

Fig. 11. Faulting patterns for an initial isotropic weak cell in the center of a grid: (a) $R = +0.12$; (b) $R = -0.2$ for two different confinement ratios. For details see [51].

negative confinement ratio yields much smaller fault angles, which are in good agreement with the above ideal effective friction theory whereby angles are calculated numerically. In these experiments it is almost impossible with a smooth envelope such as an ellipse to obtain failure zones propagating out from the central weakness. The reason for this appears to be the wide spread of failure angles possible for an elliptical case in such a stress experiment, so that the orientation angle is not focused enough, a result that has been verified by a wide range of experiments with small number of weaknesses under this type of forcing [53].

More applicable to the creation of intersecting faults in the floating pack ice are failure bands formed within a heterogeneous ice cover without Coriolis forces subjected to an idealized fixed gradient wind forcing analyzed above. In these experiments [52] a distribution of random ice strengths with spread of 50% of the mean ice strength is initially specified. For this two-dimensional system with random weaknesses, the formation of oriented lineaments requires weakening to occur. This is because localized weaknesses will typically be surrounded by stronger ice which prevents oriented failure strikes from forming. Examination of the evolution of the maximum shear zones for such an experiment [52] shows the initial state, Fig. 12(a), to relatively chaotic without any clear oriented structure. However, as weakening occurs (taken to be proportional to divergence rate) some failure points strengthen and cease deformation. Other points weaken, influencing the stress gradient in their vicinity, causing propagation of the failure zone. After a relatively small time has elapsed (~ 5 hrs) these zones (Fig. 12(b)) have propagated across the entire array. In the experiment shown here, the free drift strain ratios $\varepsilon_2/\varepsilon_1$ are $1 : 1.4$, so the approximate 60° angle between the zones is in reasonable agreement with the effective friction paradigm described above, subject to strain ratios specified [52]. After about five hours, as very weak lineated features have now formed everywhere, the non-failing regions take on a much more rigid character that the ice resembles a rigid plate with a series of long faults. Moreover, if the wind stress gradient is increased, then a higher density of failure bands is simulated (Fig. 12(c)). This result is in qualitative agreement with a scaling based upon rigid motion between faults [52]. It should be noted, however, that this scaling provides no information of the width of the faults. Overall the simulations yield results similar to the satellite observations described in Section 3.

The strong point of these simulations is that they graphically support the idealized ‘effective friction’ model presented here. That the detailed examination of the evolution of the failure shows weak regions to concentrate stress and to propagate to other weaknesses, strongly supports the proposed propagation mechanism. Moreover, although not shown here, as the fault forms the strength in the faulted region drops by orders of magnitude, in agreement with the Coulombic fault mechanism. With regard to the intersection, the angles simulated here are considerably greater than would be predicted on the basis of stress characteristics of the internal angle of friction only of the parent rheology, a procedure proposed by others. Instead, the effective friction induced by considering a finite-band zone failure, as analyzed above, fits the model simulations more closely.

The weak point of the simulations, however, is that with the fixed stress wind fields it is difficult to simulate angles as acute as seem to be observed. While there may be many reasons for this shortcoming, the most likely problem is the absence of high-frequency motion induced by inertial motions in the oceanic boundary layer acting on the ice [54]. This inertial motion can cause rapid rotation of the strain field and fluctuating divergence rate over periods of a few hours, which is likely commensurate with the time scale needed to form a fault. Due to the large magnitude of the inertial body forces in the oceanic boundary layer,

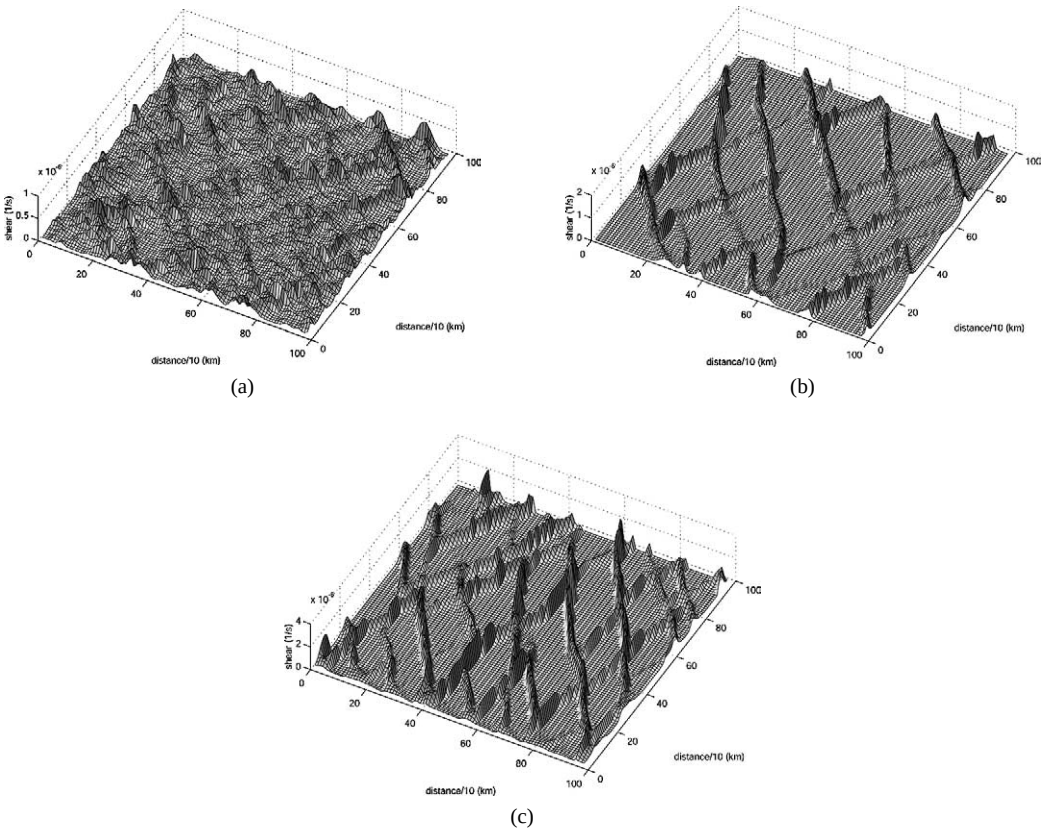

Fig. 12. (a) Maximum shear strain rate before weakening has occurred. (b) Maximum shear strain rate after 5.6 'simulation' hours. (c) Maximum shear strain rate for doubling of wind field magnitude compared to panels (a) and (b). A quarter of the 10 km resolution computational grid consisting of a 2000×2000 km^2 region is shown.

this rotation is also accompanied by a rotation of the forces acting on the ice cover. Consequently, a realistic examination of the intersecting faults in pack ice should include such high frequency effects. Encouragingly, preliminary simulations including such effects do show the capability to yield smaller intersection angles.

6. Concluding remarks

As the spatial and temporal resolution of satellite imagery continues to improve and as numerical models of the ice-ocean system approach the kilometer/sub-kilometer and the daily/sub-daily scales, it becomes increasingly important to understand the deformation of the arctic sea ice cover on all scales. In this paper we have taken the view that the ice cover, although intrinsically more complicated than a laboratory specimen, appears to obey the same basic fracture physics as the smaller body. In so doing, we presented scale-independent mechanisms that account for the brittle behavior of the cover and for the development of long, sliding lineaments that we term Coulombic shear faults, and we modeled the faults in terms of effective friction. Scale independence, although controversial, seems to be the best working hypothesis for advancing sea ice mechanics.

Acknowledgements

We acknowledge Dr. Ron Kwok of Jet Propulsion Laboratory for providing the SHEBA-SAR images in Fig. 5, obtained by the Canadian RADARSAT satellite; Dr. Jérôme Weiss of Laboratoire de Glaciologie et Geophysique de l'Environnement for discussions; and the support of the U.S. National Science Foundation and its Office of Polar Programs-Arctic Natural Sciences, through grants OPP-0328605 (EMS) and OPP-0328728 (WDH); and the support of U.S. National Oceanographic and Atmospheric Administration, grant NA17RP1400 (EMS).

References

[1] W.D. Hibler, Modeling the dynamic response of sea ice, in: J. Bamber (Ed.), Mass Balance of the Cryosphere, Cambridge University Press, Cambridge, 2003.
[2] G.A. Maykut, Large-scale heat exchange and ice production in the central Arctic, J. Geophys. Res. 87 (1982) 7971–7984.
[3] W.B. Tucker, et al., Evidence for rapid thinning of sea ice in the western Arctic ocean at the end of the 1980s, Geophys. Res. Lett. 28 (14) (2001) 2851–2854.
[4] R. Kwok, Deformation of the Arctic ocean sea ice cover between November 1996 and April 1997: a qualitative survey, in: H.H. Shen (Ed.), Scaling Laws in Ice Mechanics, Kluwer Academic, 2001, pp. 315–322.
[5] E.M. Schulson, The brittle compressive fracture of ice, Acta Metall. Mater. 38 (10) (1990) 1963–1976.
[6] E.M. Schulson, Brittle failure of ice, Engrg. Fract. Mech. 68 (17/18) (2001) 1839–1887.
[7] R.J. Evans, N. Untersteiner, Thermal cracks in floating ice sheets, J. Geophys. Res. 76 (3) (1971) 694–703.
[8] P. Wadhams, N.R. Davis, Further evidence of ice thinning in the Arctic ocean, Geophys. Res. Lett. 27 (24) (2000) 3973–3975.
[9] S. Laxon, N. Peacock, D. Smith, High interannual variability of sea ice thickness in the Arctic region, Nature 425 (6961) (2003) 947–950.
[10] J.A. Richter-Menge, S.L. McNutt, J.E. Overland, R. Kwok, Relating arctic pack ice stress and deformation under winter conditions, J. Geophys. Res. 107 (C10) (2002), art. 8040.
[11] J.A. Richter-Menge, B.C. Elder, Characteristics of pack ice stress in the Alaskas Beaufort Sea, J. Geophys. Res. 103 (C10) (1998) 21817–21829.
[12] W.F. Brace, E.G. Bombolakis, A note of brittle crack growth in compression, J. Geophys. Res. 68 (1963) 3709.
[13] F.A. McClintock, J.B. Walsh, in: 4th U.S. National Congress of Applied Mechanics, 1963.
[14] H. Horii, S. Nemat-Nasser, Compression-induced microcrack growth in brittle solids: axial splitting and shear failure, J. Geophys. Res. 90 (1985) 3105–3125.
[15] M.F. Ashby, S.D. Hallam, The failure of brittle solids containing small cracks under compressive stress states, Acta Metall. 34 (3) (1986) 497–510.
[16] M.L. Cooke, Fracture localization along faults with spatially varying friction, J. Geophys. Res. 102 (B10) (1997) 24425–24434.
[17] H. Riedel, J.R. Rice, Tensile Cracks in Creeping Solids ASTM-STP 7700 (1980) 112–130.
[18] R.A. Batto, E.M. Schulson, On the ductile-to-brittle transition in ice under compression, Acta Metall. Mater. 41 (7) (1993) 2219–2225.
[19] E.M. Schulson, O.Y. Nickolayev, Failure of columnar saline ice under biaxial compression: failure envelopes and the brittle-to-ductile transition, J. Geophys. Res. 100 (B11) (1995) 22383–22400.
[20] E.M. Schulson, S.E. Buck, The ductile-to-brittle transition and ductile failure envelopes of orthotropic ice under biaxial compression, Acta Metall. Mater. 43 (10) (1995) 3661–3668.
[21] N.P. Cannon, E.M. Schulson, T.R. Smith, H.J. Frost, Wing cracks and brittle compressive fracture, Acta Metall. Mater. 38 (10) (1990) 1955–1962.
[22] C.E. Renshaw, E.M. Schulson, Universal behavior in compressive failure of brittle materials, Nature 412 (6850) (2001) 897–900.
[23] T.J.O. Sanderson, Ice Mechanics: Risks to Offshore Structures, Graham & Trotman, London, 1988.
[24] J.P. Dempsey, Scale Effects on the Fracture of Ice, in: The Johannes Weertman Symposium, The Minerals, Metals and Materials Society, Anaheim, CA, 1996.
[25] F.E. Kennedy, E.M. Schulson, D. Jones, Friction of ice on ice at low sliding velocities, Philos. Mag. A 80 (5) (2000) 1093–1110.
[26] D. Marsan, H. Stern, R. Lindsay, J. Weiss, Scale dependence and localization of the deformation of Arctic sea ice, Phys. Rev. Lett. (2004), submitted for publication.
[27] S. Qi, E.M. Schulson, The effect of temperature on the ductile-to-brittle transition in columnar ice, in: 14th International Symposium on Ice, Balkema, Clarkson University, Potsdam, New York, 1998.
[28] H.J. Frost, M.F. Ashby, Deformation Mechanisms Maps, Permagon Press, Oxford, 1982.
[29] C. Shearwood, R.W. Whitworth, The velocity of dislocations in ice, Philos. Mag. A 64 (2) (1991) 289–302.
[30] J.W. Glen, The effect of hydrogen disorder on dislocation movement and plastic deformation in ice, Phys. Condens. Mater. 7 (1968) 43–51.
[31] J.R. Marko, R.E. Thomson, Rectilinear leads and internal motions in the ice pack of the Western Arctic ocean, J. Geophys. Res. 82 (1977) 979–987.
[32] B. Erlingsson, Two-dimensional deformation patterns in sea ice, J. Glaciology, (34) (1988) 301–308.
[33] B.A. Walter, J.E. Overland, The response of lead patterns in the Beaufort sea to storm-scale wind forcing, Ann. Glaciology 17 (1993) 219–226.
[34] R. Kwok, et al., Determination of ice age using Lagrangian observations of ice motion, IEEE Trans. Geosci. Remote Sens. 33 (2) (1995) 392–400.
[35] R.W. Lindsay, D.A. Rothrock, Arctic sea-ice leads from advanced very high-resolution radiometer images, J. Geophys. Res. – Oceans 100 (C3) (1995) 4533–4544.
[36] J.E. Overland, et al., Hierachy and sea ice mechanics: a case study from the Beaufort Sea, J. Geophys. Res. 100 (C3) (1995) 4559–4571.
[37] B.A. Walter, J.E. Overland, P. Turet, A comparison of satellite-derived and aircraft-measured regional surface sinsible heat fluxes over the Beaufort Sea, J. Geophys. Res. 100 (1995) 4584–4591.
[38] R.E. Kwok, The RADARSAT geophysical processor system, in: R. Kwok (Ed.), Analysis of SAR Data of the Polar Oceans, Springer-Verlag, Berlin, 1998, pp. 235–257.
[39] H.L. Stern, D.A. Rothrock, Open water production in Arctic sea ice: satellite measurements and model parameterizations, J. Geophys. Res. 100 (C10) (1995) 20601–20612.

[40] J.E. Overland, et al., Arctic sea ice as a granular plastic, J. Geophys. Res. – Oceans 103 (C10) (1998) 21845–21867.
[41] E.M. Schulson, Compressive shear faults within the Arctic sea ice cover on scales large and small. J. Geophys. Res. (2004), in press.
[42] D.K. Perovich, et al., Year on the ice gives climate insights, EOS, Trans. Amer. Geophys. Union 481 (80) (1999) 485–486.
[43] E.M. Schulson, D. Iliescu, C.E. Renshaw, On the initiation of shear faults during brittle compressive failure: a new mechanism, J. Geophys. Res. 104 (B1) (1999) 695–705.
[44] E.M. Schulson, W.D. Hibler, The fracture of ice on scales large and small: Arctic leads and wing cracks, J. Glaciology 37 (127) (1991) 319–323.
[45] J. Weiss, Fracture and fragmentation of ice: a fractral analysis of scale invariance, Engrg. Fracture Mech. 68 (17–18) (2001) 1975–2012.
[46] J. Weiss, Scaling of fracture and faulting of ice on earth, Surv. Geophys. 24 (2003) 185–227.
[47] S.L. McNutt, J.E. Overland, Spatial hierarchy in Arctic sea ice dynamics, Tellus Series A – Dynamic Meteorology and Oceanography 55 (2) (2003) 181–191.
[48] J.E. Overland, B.A. Walter, T.B. Curtin, P. Turet, Hierarchy and sea ice mechanics: a case study from the Beaufort sea, J. Geophys. Res. 100 (C3) (1995) 4559–4571.
[49] R.V. O'Neill, et al., A Hierarchical Concept of Ecosystems, Princeton University Press, Princeton, NJ, 1986.
[50] E.M. Schulson, Compressive shear faulting in ice: plastic vs. Coulombic faults, Acta Mater., (50) (2002) 3415–3424.
[51] W.D. Hibler, E.M. Schulson, On modeling the anisotropic failure and flow of flawed sea ice, J. Geophys. Res. 105 (C7) (2000) 17105–17120.
[52] J.K. Hutchings, W.D. Hibler, Modelling sea ice deformation with a viscous-plastic isotropic rheology, in: P. Langhorne (Ed.), Ice in the Environment, University of Otago Press, Dunedin, New Zealand, 2003, pp. 358–366.
[53] Y. Aksenov, W.D. Hibler, Failure propagation effects in an anisotropic sea ice dynamic models, in: H.H. Shen (Ed.), Scaling Laws in Ice Mechanics, Kluwer Academic, Dordrecht, 2001.
[54] R. Kwok, G.F. Cunningham, W.D. Hibler, Sub-daily sea ice motion and deformation from RADARSAT observations, Geophys. Res. Lett. 30 (2003) 2218.